(Received 6 March 2024, Accepted 8 July 2024, Scheduled 25 July 2024)

Filter Design Based on Multilayer Wide Side Coupling Structure

Wusheng Ji[1,2], Hanglin Du[1,2,*], Yingyun Tong[1,2], Xiaochun Ji[1,2], and Liying Feng[1,2]

[1] *Institute of Antenna and Microwave Techniques, Tianjin University of Technology and Education, Tianjin 300222, China*
[2] *School of Electronic Engineering, Tianjin University of Technology and Education, Tianjin 300222, China*

ABSTRACT: In this paper, three kinds of filters are designed, all of which are based on the basic multi-layer structure of microstrip-slot wire-microstrip wide edge coupling. The ultra-wideband filter is realized by three-class connection. The intermediate coupling layer of coplanar waveguide and multimode resonator is designed to realize the double broadband filter. The ultra-wideband filter is realized by using a curved T SIR structure and changing the middle coupling slot structure. The purpose of this paper is to construct a stable and easy to generalize multilayer filter design method, which can achieve broadband and high selectivity, and can realize dual passbands.

1. INTRODUCTION

As a key component of wireless communication system, microwave filter is developing rapidly in the direction of high performance, miniaturization, and low cost. The traditional design method of single-layer planar microstrip filter circuits cannot meet the actual needs. Multi-layer filter greatly reduces the volume of the filter and provides a multi-layer structure and multi-dimensional design space for the design of a microstrip filter. How to realize device miniaturization and improve the performance of the whole system based on multi-layer technology is an important content in the field of microwave filter research. At present, multi-layer technologies in microwave filters include: multi-layer substrate integrated suspended line (SISL) structure [1–3], vertically coupled substrate integrated waveguide (SIW) structure [4, 5], and low temperature cofired ceramic (LTCC) technology [6, 7]. However, the realization of multilayer microwave filters has the following problems: First, the mainstream LTCC multilayer technology is difficult to popularize. In recent years, the research on multilayer microwave filters mainly focuses on the realization of LTCC technology. Although LTCC technology can produce high performance, low price, high compactness, and high integration substrates, it also has two main disadvantages. One is that ceramics shrink to a three-dimensional direction after sintering, which affects the reliability of the circuit. The second is that the circuit module needs heat dissipation, and a heat sink must be added. Therefore, LTCC technology has higher requirements for process and equipment, and the cost is higher too. Second, low-cost, technically easy to implement design methods have not yet emerged. The higher losses and lower power processing capabilities of substrate integrated waveguides (SIWs) limit the realization of fully integrating microwave and millimeter wave components through printed circuit board (PCB) stacking. The multi-layer media integrated suspension wire structure is developed from the traditional suspended wire. Although there are many researchers, there is no universal design method that is easy to implement.

The wide-side coupling structure mainly occurs between the dielectric layers, with smaller circuit loss, smoother energy transition, and higher coupling efficiency than the traditional coupling structure. It can be applied to the design of broadband and even ultra-wideband (UWB) bandpass filters. This project is based on a basic multi-layer structure of microstrip-slot-microstrip wide-side coupling and constructs a multi-layer filter design method with a stable structure and easy popularization, which can achieve broadband and high selectivity and can achieve dual passbands.

2. REALIZATION OF AN ULTRA-WIDEBAND BANDPASS FILTER

2.1. Microstrip-Slot-Microstrip Multilayer Wide Edge Coupling Structure

The single-order multilayer wide-side coupling structure is shown in Figure 1(a), including two dielectric layers and three metal layers. The top layer and bottom layer of the coupling structure are two rectangular microstrip patches of the same size, which realize the wide side coupling in the vertical direction through the rectangular slot etched at the center of the ground surface of the middle layer.

According to [8], the reflection coefficient S_{11} of input port 1 and the insertion loss S_{21} from input port 1 to output port 2 can be obtained as follows:

$$S_{11} = \frac{1 - C^2\left(1 + \sin^2(\beta_{ef}L_1)\right)}{[\sqrt{1-C^2}\cos(\beta_{ef}L_1) + j\sin(\beta_{ef}L_1)]^2} \quad (1)$$

$$S_{21} = \frac{j2C^2\sqrt{1-C^2}\sin(\beta_{ef}L_1)}{[\sqrt{1-C^2}\cos(\beta_{ef}L_1) + j\sin(\beta_{ef}L_1)]^2} \quad (2)$$

where C is the coupling coefficient between the top layer and bottom layer; L_1 is the coupling length in the coupling struc-

* Corresponding author: Hanglin Du (duhanglin2022@163.com).

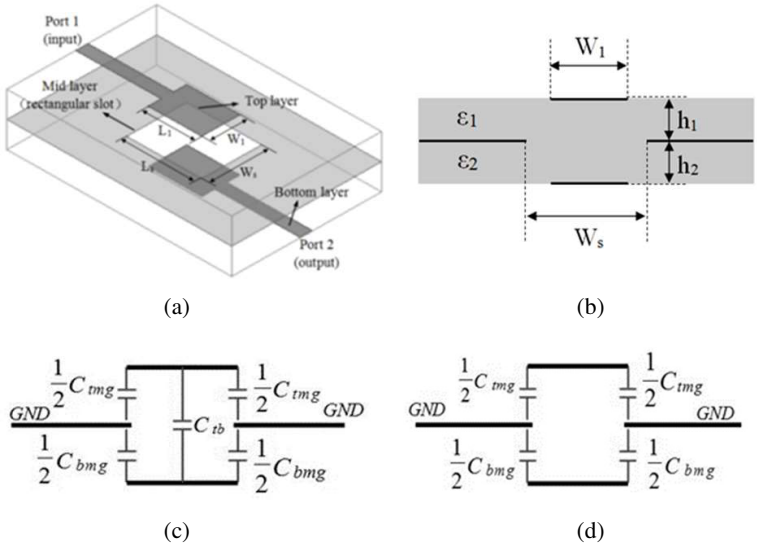

(a) (b) (c) (d)

FIGURE 1. Microstrip-slot-microstrip multi-layer wide-side coupling structure diagram. (a) Three-dimensional structure diagram; (b) Schematic diagram of cross-section structure; (c) Odd mode equivalent circuit; (d) Even mode equivalent circuit.

ture, that is, the length of the top and bottom rectangular microstrip patches; β_{ef} is the equivalent phase constant; L_1 is approximately equal to the quarter waveguide wavelength at the center frequency of the filter passband (6.10 GHz).

Figure 1(b) shows the cross-section diagram of the wide-side coupling structure. Figure 1(c) and Figure 1(d) are the odd-mode equivalent circuit and even-mode equivalent circuit of the wide-side coupling structure. The coupling coefficient between the top and bottom microstrip patches [9] is:

$$C = \sqrt{\frac{Z_{be}Z_{bo}}{Z_{te}Z_{to}}}\frac{Z_{te}-Z_{to}}{\sqrt{(Z_{be}+Z_{bo})(Z_{te}+Z_{to})}} \tag{3}$$

where Z_{to} and Z_{bo} are the odd-mode equivalent impedances of the top and bottom microstrip patches, respectively, and Z_{te} and Z_{be} are the even-mode equivalent impedances of the top and bottom microstrip patches, respectively.

2.2. Multi-Class Linkage of a Wide-Side Coupling Structure

To achieve the best performance of the filter, it is necessary to realize the multi-class cascade of the wide-side coupling structure. Figure 2 shows the wide-side coupling structure of the two-class cascade, and two coupling structures are connected by a microstrip line of length L_2 (assuming that its phase constant is β_m). The characteristics of the two-class cascade structure can be analyzed through the S parameter performance, and the two-class cascade characteristics can also be extended to any order. It can be seen from the S parameter that L_2 has an important impact on the transmission characteristics of the circuit, so to make the filter have a good impedance match, the selection of L_2 is very important, and its optimal value is $\lambda_m/8$ [8]. At the same time, to avoid unnecessary coupling, the characteristic impedance of microstrip lines between cascaded structures should preferably be about 50 Ω [10].

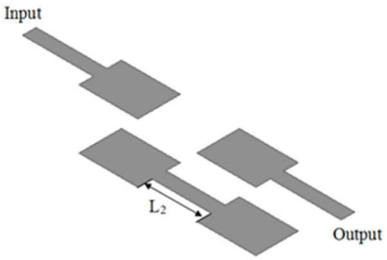

FIGURE 2. Schematic diagram of the wide-side coupling structure of the two-class cascade.

2.3. Ultra-Wideband Bandpass Filter

2.3.1. Structural Model and Optimization

This model is a three-class cascade wide-side coupling structure, and the middle layer uses a large rectangular slot formed by merging the original three small rectangular slots [11], as shown in Figure 3. In the cascade area of the top and bottom microstrip structures of the ultra-wideband filter circuit, the rectangular microstrip patch connected by 50 Ω microstrip line forms a half-wavelength step impedance resonator (SIR), where the length of the open-circuit microstrip line with low impedance at both ends is L_1; the width is W_1; the characteristic impedance is Z_1; and the electrical length is θ_1. The length of the middle high-impedance microstrip line is L_2; the width is W_2; and its characteristic impedance and electrical length are Z_2 and $2\theta_2$, respectively. The impedance ratio R_z and electrical length ratio α of half-wavelength SIR are:

$$R_z = Z_1/Z_2 = \tan\theta_1 \tan\theta_2 \tag{4}$$

$$\alpha = \theta_1/(\theta_1+\theta_2) \tag{5}$$

The R_z and α can affect the resonance performance of the circuit.

HFSS-15 simulation software is used to verify and study the factors that affect the resonance characteristics and passband

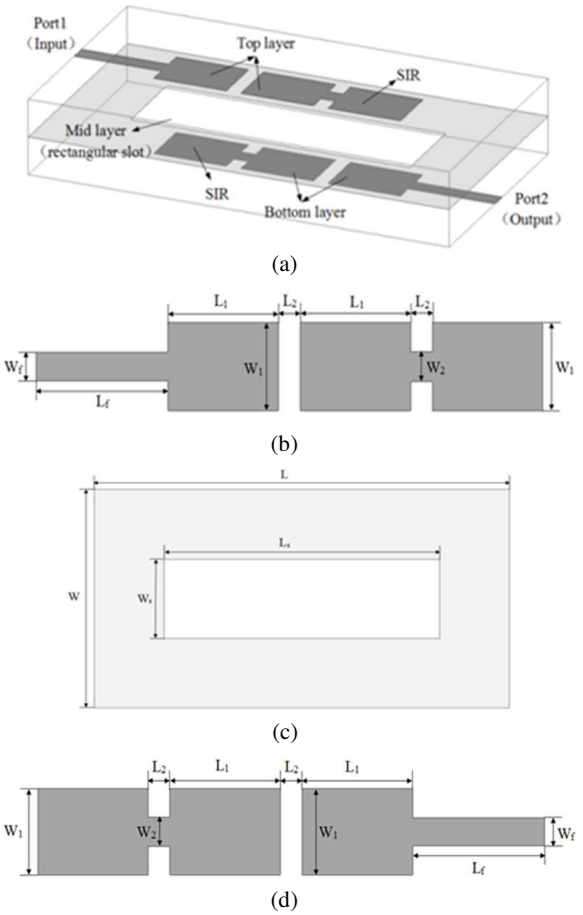

FIGURE 3. (a) Three-class connected ultra-wideband filter; (b) Schematic diagram of top structure; (c) Schematic diagram of middle structure; (d) Schematic diagram of bottom structure.

bandwidth of the filter circuit. As shown in Figure 4, with the increase of L_1, the resonance points f, f_1, and f_2 shift to the low-frequency band, indicating that changing L_1 can adjust the operating frequency band of the circuit, and the absolute bandwidth of the resonance points f and f_1 is only about 3 GHz, which is far from enough for the ultra-wideband characteristics, so the passband bandwidth of the filter should be expanded as far as possible.

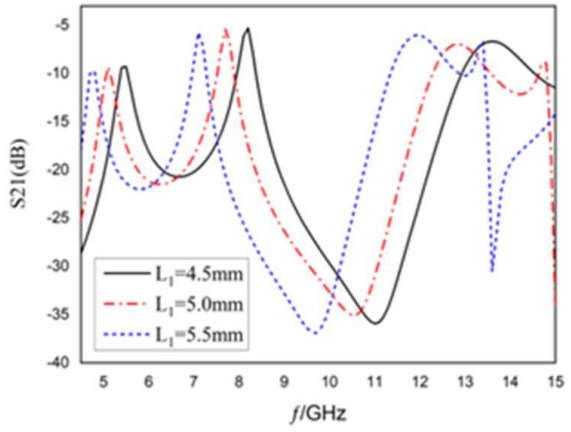

FIGURE 4. Effect of L_1 on resonance point.

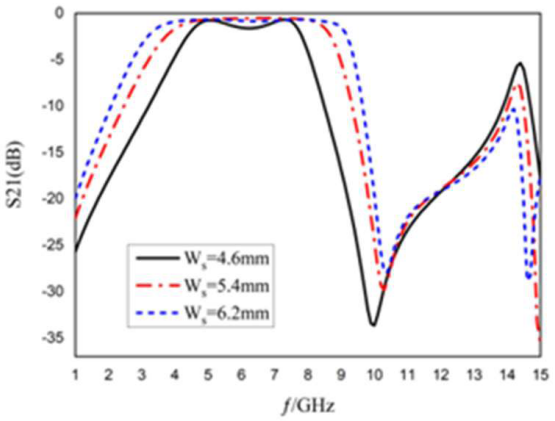

FIGURE 5. Impact of W_S on in-band S_{21}.

In this filter structure, the structure parameters (L_S and W_S) of the rectangular slot in the middle layer have a great influence on the passband bandwidth. Figure 5 shows the influence of W_S on the in-band S_{21}. It can be seen that with the increase of W_S, the central frequency of the passband almost does not change, but the bandwidth increases. When W_S is 6.2 mm, the fractional bandwidth of the passband reaches 100%. Therefore, using this property, the passband bandwidth can be adjusted by adjusting the structural parameters of the rectangular slot in the middle layer, which reflects good design flexibility.

2.3.2. Prototype Production and Result Analysis

After the optimization of structural parameters in HFSS software, the designed filter circuit prototype is processed and manufactured, and the filter prototype is tested using the vector network analyzer AV3629. The circuit prototype uses two layers of RO4003C dielectric substrate with a thickness of 0.508 mm. A dissipation factor is 0.0029, and an overall circuit size reaches 29 mm × 16 mm × 1.016 mm. A photo of the prototype and the simulation and test results of the filter circuit are shown in Figure 6. The optimized structural parameters are as follows: $L_1 = 5$ mm, $L_2 = 1$ mm, $L_S = 19.2$ mm, $W_f = 1.15$ mm, $W_1 = 4$ mm, $W_2 = 1.2$ mm, $W_S = 6.2$ mm.

As can be seen from Figure 6, the filter has ultra-wideband characteristics, operating at 3.05–9.17 GHz; the center fre-

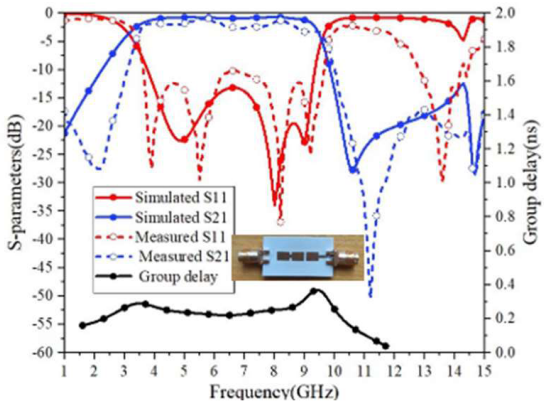

FIGURE 6. Simulation and test results of UWB filter prototype.

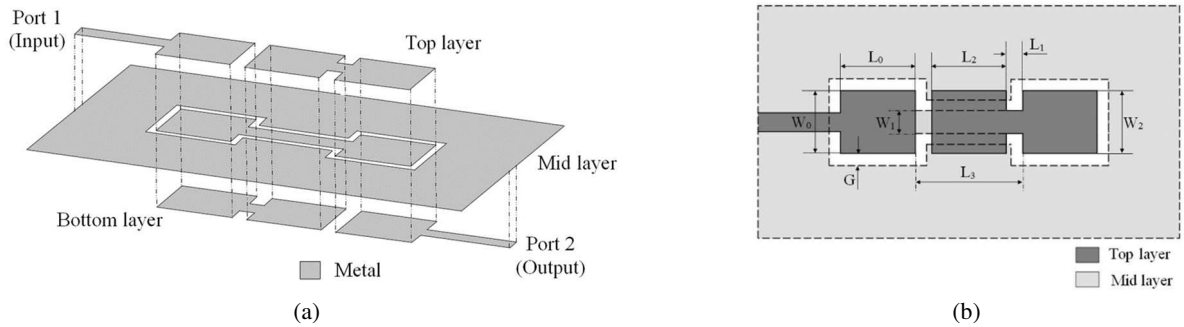

FIGURE 7. Structure diagram of dual broadband bandpass filter. (a) Side view of the structure; (b) Top view of the structure.

quency of the passband is 6.10 GHz; and the fractional bandwidth reaches 100.3%. From the simulation results, there are three transmission poles in the band. The insertion loss is better than -0.95 dB, and the return loss is better than -13 dB. The filter contains a transmission zero at 10.6 GHz in the upper stopband, and the out-of-band rejection at 15 GHz is better than -13 dB. The in-band group delay varies from 0.21 ns to 0.34 ns, which indicates that the linear characteristics of the filter are good. There is a certain deviation between the test results and simulation results, but they are consistent. The out-of-band rejection in the upper stopband 15 GHz is better than -17 dB, and the cut-off edge of the lower stopband is steeper than the simulation results, reflecting the good passband selection performance and out-of-band rejection ability of the filter.

3. REALIZATION OF DUAL WIDEBAND FILTER

3.1. Construction of Dual Broadband Bandpass Filter by Ultra-Wideband Splitting

Based on the ultra-wideband filter, the intermediate coupling layer is designed as a coplanar waveguide-multimode resonator (CPW-MMR) from a rectangular slot, and additional transmission zeros are introduced in the passband. One ultra-wideband is split into two passbands, and a dual wideband bandpass filter is constructed, as shown in Figure 7 [11]. In Figure 7, CPW-MMR is composed of one high-impedance CPW at the center and two low-impedance open-circuit CPWs at the left and right sides, with uniform slot width G. The length L of two low-impedance open-circuit CPWs is about a quarter of the waveguide wavelength of the center frequency of the first passband. The length L_3 of the central high impedance CPW is about half of the waveguide wavelength. The microstrip structure at the top or bottom of the circuit is oddly symmetrical about the positive center of the circuit, and both contain a rectangular microstrip patch and a half-wavelength SIR. The half-wavelength SIR consists of a high-impedance microstrip line in the middle (the length is L_1; width is W_1; characteristic impedance is Z_1; and electrical length is $2\theta_1$) and two low-impedance open-circuit microstrip lines at the left and right ends (the length is L_2; width is W_2; characteristic impedance and electrical length are Z_2 and $2\theta_2$, respectively). Figure 7(b) shows only the top view of the top and middle layers (the bottom microstrip structure has been omitted).

To suppress the strong harmonic response near the stopband (10–15 GHz) on the second passband, the initial structure of the filter is optimized: load an open-circuit single-node microstrip line [12] on the microstrip feeder at the input and output ends, and adjust L (the CPW-MMR structure of the middle layer remains unchanged). Figure 8 shows the top view of the top and middle layer structure of the improved filter (the bottom microstrip structure is omitted).

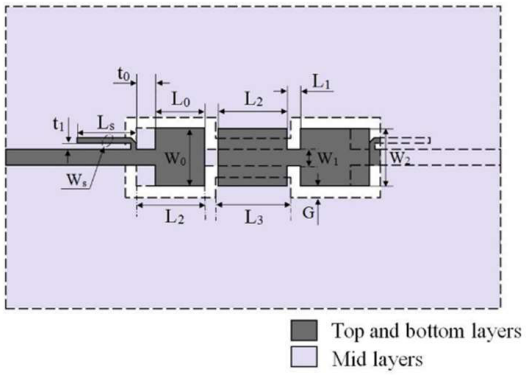

FIGURE 8. Top and middle layer structure of the improved filter.

3.2. Prototype Production and Results Analysis

After the optimization of structural parameters in HFSS software, the filter circuit prototype is processed and manufactured, and the circuit prototype is tested using the vector network analyzer AV3629. The actual circuit uses an RO4003C dielectric substrate. The thickness of the two layers of the dielectric substrate is 0.508 mm, and the overall size of the circuit reaches 36 mm $\times$22 mm$\times$1.016 mm. The optimized structural parameters are as follows: $W = W_2 = 4.2$ mm, $W_1 = 1.2$ mm, $L = 3.6$ mm, $L_1 = 1$ mm, $L_2 = 5$ mm, $L_3 = L_2 + 2L_1 = 7$ mm, $G = 0.8$ mm, $L_S = 4.36$ mm, $W_S = 0.3$ mm, $t = 1.4$ mm, $t_1 = 0.11$ mm. Both simulation and test results are shown in Figure 9, where the solid line is the simulation results, and the dashed line is the measured ones [11].

As can be seen from Figure 9, the filter contains two broadband bands: the center frequency of the first passband is 3.6 GHz, and the fractional bandwidth reaches 95.1%, including China's 5G communication planning frequency band. The center frequency of the second passband is 8.4 GHz, and the

TABLE 1. Performance comparison of dual wideband bandpass filters.

Ref. No.	Center frequency (GHz)	Fractional bandwidths	Size (mm^3)
[2]	2.45, 5.13	58.3%, 17.8%	$20.48 \times 21.25 \times 2.53$
[3]	2.4, 5.2	45.43%, 21.64%	$32 \times 22.86 \times 5.454$
[13]	3.32, 5.32	27.71%, 19.17%	$10 \times 21.8 \times 0.508$
Work II	3.6, 8.4	95.1%, 36.8%	$36 \times 22 \times 1.218$

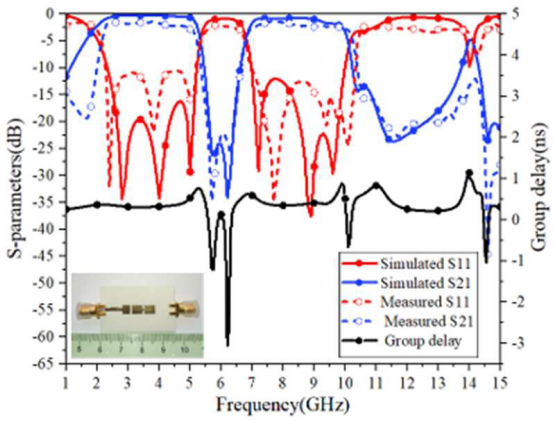

FIGURE 9. Dual wideband filter circuit simulation and test results.

fractional bandwidth reaches 36.8%, which belongs to the B5G band. The center frequency of the stopband is 6.0 GHz, and the fractional bandwidth reaches 26.7%. The group delay of the first passband is in the range of 0.307–0.737 ns. The group delay of the second passband is in the range of 0.348–0.878 ns. Good linearity is shown in both passbands. This resonance characteristic indicates that the performance of the two passbands can be adjusted by changing the electrical length ratio of the half-wavelength SIR, and the stopband bandwidth between the passbands is almost unchanged. The bandwidth of the two passbands is basically unchanged, reflecting good design flexibility [11]. The deviation between the test and simulation results is about 7 dB, which is mainly caused by the introduction error of the manual welding SMA joint and can be reduced by calibration. In addition, the upper stopband edge of the second passband of the circuit is steep, which reflects good passband selection performance.

The comparison between the dual wideband filter (Work II) and other literatures is shown in Table 1. As can be seen from Table 1, compared with other literatures, the two broadband bands of the dual-band broadband bandpass filter have higher frequencies. Both the first and second passband bandwidths are wide. Changing the parameters of CPW can make the center frequency of the passband and stopband shift up or down, but the bandwidths of the passband and stopband remain unchanged, and the design freedom is high.

4. THE IMPLEMENTATION OF A CURVED T-TYPE BROADBAND FILTER

4.1. Curved T-Type Ultra-Wideband Filter

Based on the ultra-wideband filter (Figure 3), the rectangular microstrip patch in the top and bottom topology is designed as a curved T-shaped microstrip patch, and the half-wavelength step impedance resonator (SIR) in the top and bottom layers is designed as a curved T-shaped SIR, and the middle coupling layer replaces the rectangular coupling slot with a circular coupling slot to form a new type of microstrip-slot type wide-side coupling resonator. The curved T-shaped ultra-wideband filter is constructed [1], as shown in Figure 10.

Figure 10 shows an ultra-wideband filter realized by the cascade of three coupled resonant units. Figure 10(b) shows the top layer structure. The curved T-shaped microstrip structure is formed by removing two small semicircles from a large semicircle microstrip patch to form two grooves, and then directly connected with the microstrip, where w_1 is the width of the microstrip line, and O and D_m are the center and diameter of the large semicircle microstrip patch, respectively. The relationship between circuit parameters meets:

$$D_{m1} = (D_m - w_1)/2 \quad (6)$$

$$D_{m2} = (D_m - w_2)/2 \quad (7)$$

where D_S is the coupling slot diameter.

Figure 10(c) shows the structure of the intermediate coupling layer, where O_1, O_2, and O_3 are the center of the resonator coupling area; D_S is the diameter of the circular coupling groove in the intermediate layer; and d is the distance between the adjacent centers of the coupling area.

Through simulation and optimization, the structure parameters of the filter circuit are $w_1 = 1.15$ mm, $D_m = 4.5$ mm, $D_S = 6.1$ mm, $l_a = 3.3$ mm, and $h_1 = h_2 = 0.508$ mm. The S parameters and group delay of the UWB filter obtained by simulation are shown in Figure 11 [1]. The center frequency of the passband f is 7.1 GHz; the upper and lower frequency points of the passband are 3.7 GHz and 10.5 GHz respectively; and the 3 dB fractional bandwidth can be calculated to be 96%. The in-band return loss S_{11} is less than -10 dB, and other frequency bands are better than -15 dB. The in-band group delay varies from 0.15 ns to 0.35 ns. At the same time, there are 6 transmission poles in the band, which strengthens the circuit coupling.

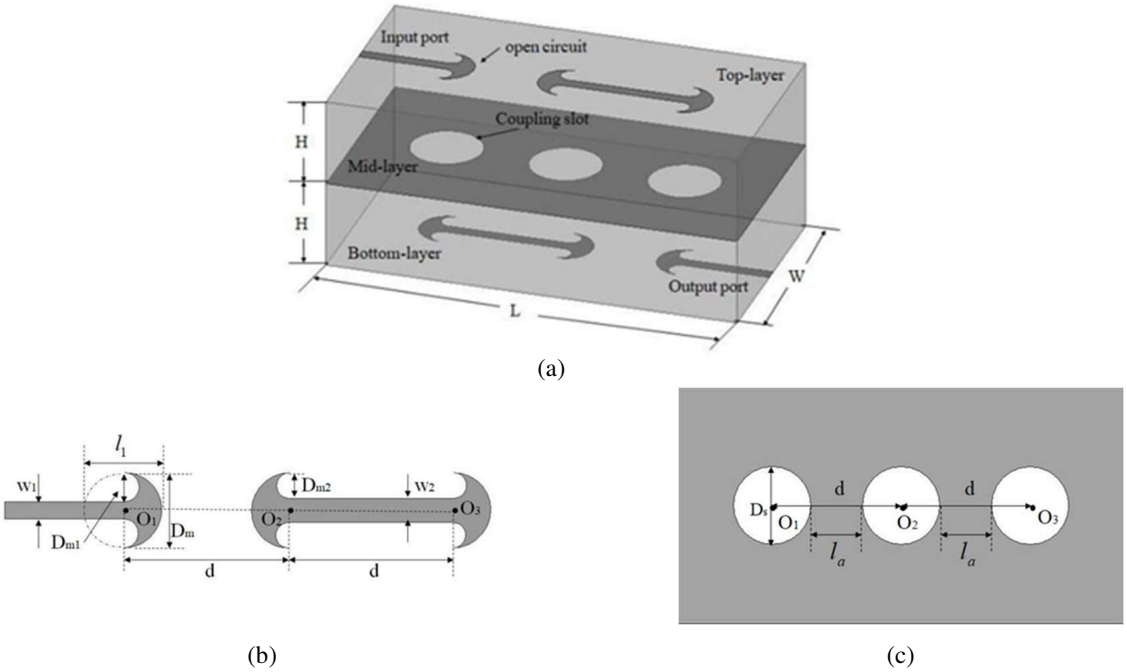

FIGURE 10. Filter circuit simulation and test results. (a) Overall circuit structure diagram; (b) The upper and lower curved T-shaped microstrip structure; (c) Intermediate layer coupling groove structure.

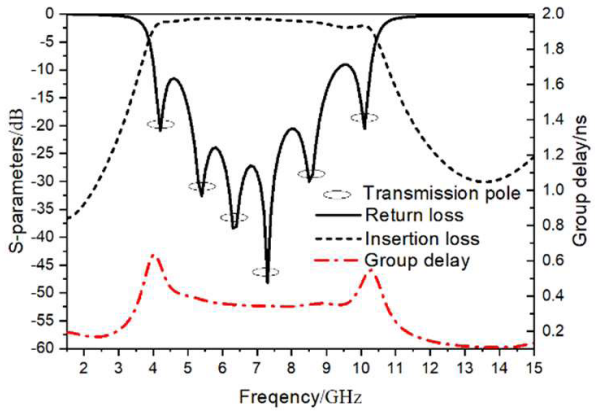

FIGURE 11. S-parameter and group delay of ultra-wideband filter.

4.2. Curved T-Type Broadband Filter

4.2.1. Structural Model and Principle Analysis

Based on the curved T-type ultra-wideband filter (Figure 10), by reducing the distance between the resonators, make the resonators close to each other, make the circular coupling groove of the middle coupling layer partially overlap, and connect into a 'sugar gourd' shaped coupling groove, but the curved T-type microstrip and curved T-type SIR of the top layer (bottom layer) do not overlap, forming a new type of microstrip-slot type wide-side coupling broadband filter, as shown in Figure 12.

The top-level topology of the curved T-shaped microstrip structure is consistent with Figure 10(b), where w_1 is the width of the microstrip line; O and D_m are the center and diameter of the large semicircular microstrip patch; D_{m1} is the diameter of each curved T-shaped microstrip patch; and the relationship between D_{m21} and D_{m22} is as follows:

$$D_{m21} = (D_{m1} - w_1)/2 \tag{8}$$

$$D_{m22} = (D_{m1} - w_2)/2 \tag{9}$$

The structure of the intermediate coupling layer is shown in Figure 12(b). In order not to overlap the two curved T-shaped microstrip patches and avoid other unnecessary circuit effects, it is necessary to ensure that $d > D_{m1}$, the center of the middle layer coupling slot, and the center of the curved T-shaped microstrip patch are on the same vertical line. The surface current distribution of the top curved T-shaped microstrip is shown in Figure 13. The induced current is mainly distributed on the input microstrip line and the microstrip with a width of W_2. In the wide-side coupling structure of the microstrip-slot type, the relationship between the coupling coefficient between the upper and lower microstrips and the odd and even mode impedances is as follows [14]:

$$C = \frac{Z_{oe} - Z_{oo}}{Z_{oe} + Z_{oo}} \tag{10}$$

where Z_{oe} and Z_{oo} are the even-mode impedance and odd-mode impedance of the circuit, respectively. This value can

TABLE 2. Impact of w_2 on Z_{oo}, Z_{oe}, C, and fractional bandwidth (FBW).

w_2 (mm)	1	1.5	2
Z_{oo} (Ω)	35.5	31.2	28.5
Z_{oe} (Ω)	70.4	80	87.8
C	0.33	0.44	0.51
FBW (1.5 dB)	41.6%	53.2%	59.6%

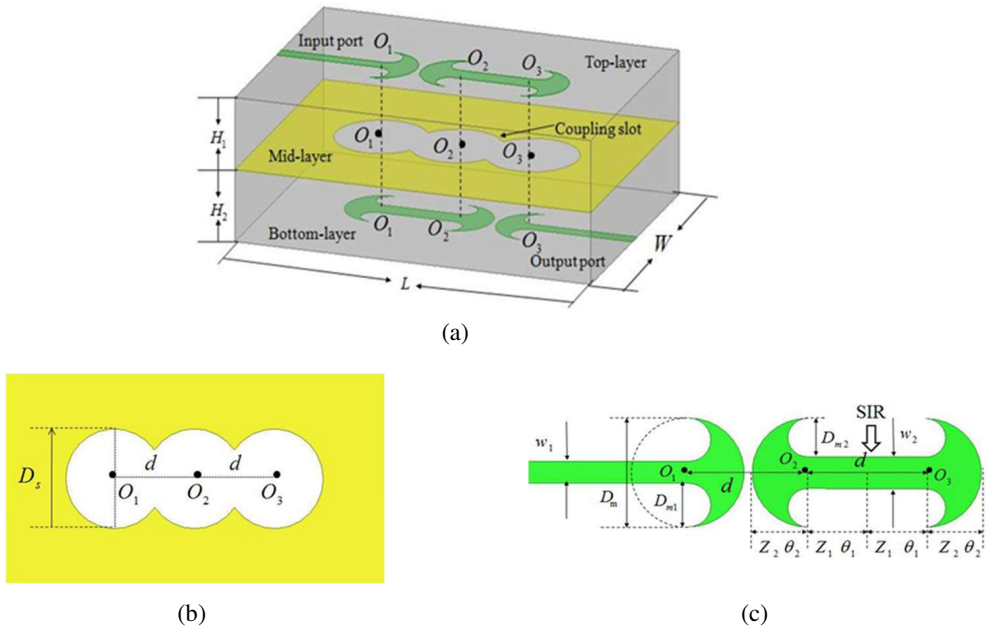

FIGURE 12. Structure diagram of bent T-type broadband filter. (a) 3D three-dimensional structure diagram; (b) Schematic diagram of the top structure; (c) Schematic diagram of the middle floor structure.

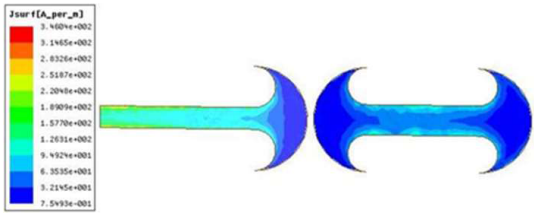

FIGURE 13. Current distribution of top curved T-shaped structure.

be obtained by using HFSS-15 simulation software by setting a differential pair at the excitation port of the two-port network. Change w_2 to obtain circuit S parameters as shown in Figure 14, and the corresponding circuit characteristic parameters are shown in Table 2. It can be seen that the increase of w_2 increases the coupling surface between the upper and lower microstrips; the coupling coefficient increases; the lower stopband of the bandwidth does not change; the upper stopband shifts towards the high-frequency band; and the overall bandwidth of the circuit also increases.

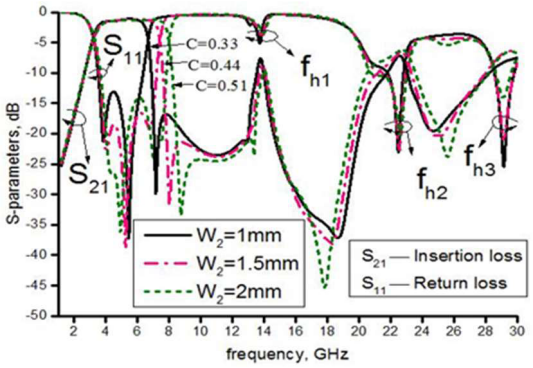

FIGURE 14. Effect of w_2 on bent T-type broadband filter filter.

4.2.2. Harmonics by Half-Wavelength SIR

In Figure 12(b), two curved T-shaped microstrip patches connected by w_2 constitute a half-wavelength SIR resonator. Z_1, Z_2, θ_1, and θ_2 are the characteristic impedance and equivalent electrical length of each section of the microstrip, respectively. The half-wavelength SIR resonance condition is:

$$\theta_0 = \theta_1 = \theta_2 = \arctan\sqrt{Z_r} \tag{11}$$

where θ_0 is the equivalent electrical length corresponding to the center frequency f, and the impedance ratio $Z_r = Z_2/Z_1$. When w_2 increases, Z_r increases, and f also increases. The first three parasitic resonant frequencies of the filter circuit are f_{h1}, f_{h2}, and f_{h3}, respectively. The relationship between f and Z_r is as follows:

$$\frac{f_{h1}}{f_0} = \frac{\pi}{2\arctan\sqrt{Z_r}} \tag{12}$$

$$\frac{f_{h2}}{f_0} = 2\left(\frac{f_{h1}}{f_0}\right) - 1 \tag{13}$$

$$\frac{f_{h3}}{f_0} = 2\left(\frac{f_{h1}}{f_0}\right) \tag{14}$$

According to formulas (12), (13), and (14), Z_r, f_{h2}, and f_{h3} can be calculated as shown in Table 3. The calculation results are consistent with the simulation data in Figure 14. It can be seen that with the increase of w_2, f_{h2} is unchanged; the bandwidth and position of the second parasitic passband are unchanged; and f_{h2} and f_{h3} both are above 20 GHz, which ensures that the upper stopband can be extended to a higher frequency band. At the same time, because the half-wavelength SIR resonator can suppress the out-of-band parasitic passband, the circuit has no parasitic passband formation at f_{h1}.

TABLE 3. Impact of w_2 on f_0, f_{h1}, f_{h2}, f_{h3} and Z_r.

W_2 (mm)	f (GHz)	f_{h1} (GHz)	f_{h2} (GHz)	f_{h3} (GHz)	Z_r
1	4.95	13.7	22.3	27.2	0.4
1.5	5.45	13.9	22.4	27.3	0.5
2	5.7	14.2	22.5	28.2	0.54

TABLE 4. Performance comparison of broadband BPFs.

Ref. No.	Center Frequency (GHz)	Fractional Band widths	Insertion Loss (dB)	Size (mm^3)
[15]	4.015	38.06%	0.947	/
[16]	535	54.2%	0.75	7×6.78×2.385
[17]	5.41	54.9%	0.89	7×7.58×0.25
Work I	6.1	100.3%	0.95	29×16×1.016
Work III	54	57.7%	1.5	36×22×1.218

4.2.3. Prototype Production and Results Analysis

Figure 15 is the physical picture of the broadband filter, and the overall size of the physical circuit is $W \times L = 15\,\text{mm} \times 27.6\,\text{mm}$. To ensure that the input port is $50\,\Omega$, the structure parameters of the filter circuit are $w_1 = 1.15\,\text{mm}$, $w_2 = 1.16\,\text{mm}$, $D_m = 5.5\,\text{mm}$, and $d = 5.8\,\text{mm}$. The simulated and measured results are shown in Figure 16. There is an error about 0.15 GHz between the communication bandwidth of the physical circuit test and the simulation results, which is caused by insufficient manufacturing accuracy and the error caused by the introduction of coaxial connectors. The center frequency of the physical circuit is 5.48 GHz, and the 1.5 dB fractional bandwidth is 57.7%. The insertion loss of the circuit is less than $-1.5\,\text{dB}$, and there is a transmission zero point outside the band, so the attenuation outside the band is good. The return loss of the circuit is better than $-17\,\text{dB}$, and the stopband on the circuit extends to more than 20 GHz.

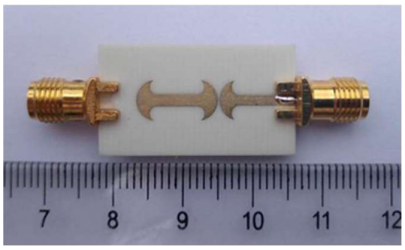

FIGURE 15. Physical photo of the broadband filter.

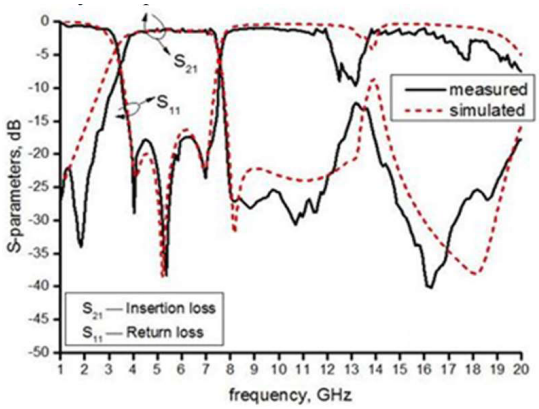

FIGURE 16. Comparison of S-parameters between test and simulation results of wideband filter.

The ultra-wideband broadband filter (Work I) and curved T-type broadband filter (Work III) are compared with other literatures, as shown in Table 4. As can be seen from Table 4, compared with other works, the two wideband filters designed in this paper have wider passband bandwidths in the frequency range.

5. PCB PRESSING PROCESS

In this study, ultra-wideband filter, double-wideband band-pass filter, and bent T-type broadband filter are all prepared by PCB pressing process, and their actual processing structure is shown in Figure 17. The prototype adopts two layers of RO4003C dielectric substrate produced by Rogers with the same thickness. In addition, to ensure the reliability of the bonding of the upper and lower dielectric substrates, two layers of RO4450B semi-curing sheets with the same thickness were selected to press the two layers of dielectric substrates. The dielectric properties of RO4450B semi-cured sheet are close to that of RO4003C, and the thickness is very small (0.101 mm). The semi-cured sheet will be softened by heat during pressing, and the effect of pressing on the two-layer dielectric substrate is not significant. This PCB preparation process has a low price, low circuit production cost, mature technology, and is easy to promote.

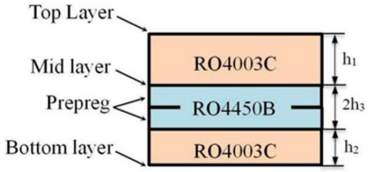

FIGURE 17. Structure diagram of three-layer filter pressing process.

6. CONCLUSION

Based on the basic multi-layer structure of microstrip-slot-microstrip wide-side coupling, the top (bottom) layer is designed as a combination structure of feed microstrip and half-wavelength SIR to build an ultra-wideband filter. The intermediate coupling slot is designed as a CPW-MMR structure, which builds a dual broadband filter. By transforming the top (bottom) rectangular microstrip structure into a curved T-shaped microstrip structure, and the middle coupling layer into a circular coupling slot, a new ultra-wideband filter is realized. The above three filters are prepared by PCB pressing process, which is simple and has low cost. All three filters can work in a sub-6 GHz frequency band, realizing broadband and high selectivity. In this paper, a design method of multilayer filter with a stable structure and easy to popularize is constructed, which has application prospects in the 5G communication field.

ACKNOWLEDGEMENT

This work is supported by the Natural Science Foundation of Tianjin, China (18JCYBJC16400), Tianjin Key Projects of Research and Development and Science and Technology Support in 2020 (20YFZCGX00700), and Tianjin Enterprise Science and Technology Commissioner Project in 2022 (22YDTPJC00330).

REFERENCES

[1] Xiao, J.-K., X.-Y. Yang, and X.-F. Li, "A 3.9 GHz/63.6filtering power divider using self-packaged SISL," *IEEE Transactions on Circuits and Systems II: Express Briefs*, Vol. 68, No. 6, 1842–1846, 2021.

[2] Feng, T., K. Ma, and Y. Wang, "A dual-band coupled line power divider using SISL technology," *IEEE Transactions on Circuits and Systems II: Express Briefs*, Vol. 68, No. 2, 657–661, 2021.

[3] Chu, Y., K. Ma, Y. Wang, and F. Meng, "A self-packaged low-loss and compact SISL DBBPF with multiple TZs," *IEEE Microwave and Wireless Components Letters*, Vol. 29, No. 3, 192–194, 2019.

[4] Guo, J., B. You, X. H. Zhang, and G. Q. Luo, "Compact dual-band filter using interleaved folded half-mode substrate integrated waveguide resonator," *IET Microwaves, Antennas & Propagation*, Vol. 13, No. 11, 1773–1776, 2019.

[5] Ghiotto, A., J.-C. Henrion, T. Martin, J.-M. Pham, and V. Armengaud, "AFSIW-to-microstrip directional coupler for high-performance systems on substrate," in *2020 IEEE/MTT-S International Microwave Symposium (IMS)*, 173–176, Los Angeles, CA, USA, 2020.

[6] Tang, W., R. Xu, and L. Zhao, "A miniaturized bandpass filter based on LTCC," in *2023 International Conference on Microwave and Millimeter Wave Technology (ICMMT)*, 1–3, Qingdao, China, 2023.

[7] Huang, X., X. Zhang, L. Zhou, J.-X. Xu, and J.-F. Mao, "Low-loss self-packaged Ka-band LTCC filter using artificial multi-mode SIW resonator," *IEEE Transactions on Circuits and Systems II: Express Briefs*, Vol. 70, No. 2, 451–455, 2023.

[8] Abbosh, A. M., "Planar bandpass filters for ultra-wideband applications," *IEEE Transactions on Microwave Theory and Techniques*, Vol. 55, No. 10, 2262–2269, 2007.

[9] Abbosh, A., M. Bialkowski, and S. Ibrahim, "Ultra-wideband bandpass filters using broadside-coupled microstrip-coplanar waveguide," *IET Microwaves, Antennas & Propagation*, Vol. 5, No. 7, 764–770, 2011.

[10] Ji, X.-C., W.-S. Ji, L.-Y. Feng, Y.-Y. Tong, and Z.-Y. Zhang, "Design of a novel multi-layer wideband bandpass filter with a notched band," *Progress In Electromagnetics Research Letters*, Vol. 82, 9–16, 2019.

[11] Ji, W.-S., Y.-Y. Tong, Z.-Y. Zhang, W. Dai, and Y.-J. Li, "Dual-wideband bandpass filter using multilayer broadside-coupled structure," *Microwave and Optical Technology Letters*, Vol. 62, No. 11, 3451–3457, 2020.

[12] Zhang, S. and L. Zhu, "Compact and high-selectivity microstrip bandpass filters using triple-/quad-mode stub-loaded resonators," *IEEE Microwave and Wireless Components Letters*, Vol. 21, No. 10, 522–524, 2011.

[13] Li, J., S.-S. Huang, and J.-Z. Zhao, "Compact dual-wideband bandpass filter using a novel penta-mode resonator (PMR)," *IEEE Microwave and Wireless Components Letters*, Vol. 24, No. 10, 668–670, 2014.

[14] Abbosh, A. M., "A compact UWB three-way power divider," *IEEE Microwave and Wireless Components Letters*, Vol. 17, No. 8, 598–600, 2007.

[15] Yang, L. and R. Gómez-García, "Multilayered balanced wideband bandpass filter with high filtering selectivity," in *2021 IEEE MTT-S International Microwave Filter Workshop (IMFW)*, 17–19, Perugia, Italy, 2021.

[16] Messaoudi, E. M., J. D. Martínez, and V. E. Boria, "Miniaturized ultra-wideband bandpass filter based on substrate integrated quasi-lumped resonators," in *2021 IEEE MTT-S International Microwave Filter Workshop (IMFW)*, 201–203, Perugia, Italy, 2021.

[17] Messaoudi, E. M., J. D. M. Perez, and V. E. Boria, "Compact substrate integrated waveguide wideband bandpass filter with post-manufacturing tuning capabilities," *IEEE Access*, Vol. 11, 2327–2341, 2023.